Atomically dispersed tungsten on metal halide monolayer as a ferromagnetic Chern insulator

Atomically dispersed tungsten on metal halide monolayer as a ferromagnetic Chern insulator

Chengxi Huang,[1] Kaiming Deng,[1] Jian Zhou,[2,*] and Erjun Kan[1,†]

[1]*Department of Applied Physics and Institution of Energy and Microstructure, Nanjing University of Science and Technology, Nanjing, Jiangsu 210094, People's Republic of China*

[2]*Center for Advancing Materials Performance from the Nanoscale, State Key Laboratory for Mechanical Behavior of Materials, Xi'an Jiaotong University, Xi'an 710049, China and Research Laboratory of Electronics, Massachusetts Institute of Technology, Cambridge, Massachusetts 02139, USA*

(Received 14 June 2018; revised manuscript received 22 August 2018; published 14 September 2018)

Although the quantum anomalous Hall (QAH) effect has been experimentally observed in several magnetically doped topological insulators, up to now, it only survives at a very low temperature. More suitable candidate QAH insulators that can work at high temperature are much desired. Here, we propose an experimentally feasible way to realize a robust QAH insulator: atomically dispersed transition metals (e.g., W) on a two-dimensional porous metal halide normal insulator (e.g., InI_3), which has been developed as a state-of-the-art chemical technology broadly adopted for homogeneous catalysis. Based on the first-principles calculations, we predict that the atomic W embedded in an InI_3 monolayer forms an intrinsic ferromagnetic QAH insulator, which exhibits robust uniform out-of-plane ferromagnetic order up to ∼160 K and a topologically nontrivial band gap of 56 meV with a nonzero Chern number ($|C| = 2$). We also study its magneto-optical Kerr effect and collective plasma excitation modes, which may help for further experimental verifications and measurement of interesting physical features of Dirac-like electronic dispersion. Our results introduce a feasible method to obtain the QAH effect, which may motivate intensive experimental interest in this field.

DOI: 10.1103/PhysRevB.98.115424

I. INTRODUCTION

The quantum anomalous Hall (QAH) effect is a prominent topological electronic phase that arises in a time-reversal symmetry-breaking two-dimensional (2D) material, which also has a strong spin-orbit coupling (SOC) [1–4]. As a quantized response of a transverse spin-polarized current to an electric field in the absence of an external magnetic field, a QAH insulator is featured as chiral gapless edge states with insulating bulk, and is characterized by a nonzero Chern number (C) of its electronic structure in the reciprocal space, which accounts the number of gapless edge states with linear dispersion. Thus, a QAH insulator is also termed as Chern insulator. This chiral edge state is topologically protected and robust against any impurity perturbations, so that it holds potential to work in future spintronic devices with low consumption and dissipation. To achieve this goal, a feasible Chern insulator with abundant gapless edge states ($|C| > 1$) that can work at high temperature is much desired.

Although quite a few intrinsic QAH insulators have been theoretically predicted [5–12], the widely used method to realize the QAH effect in experiments is doping magnetic impurities (e.g., transition metals) into a topological insulator [13–20]. Once the inherent time-reversal symmetry is broken, a chiral edge state can be expected. Unfortunately, similar to the conventional dilute magnetic semiconductors, the magnetic moments in such systems are usually very small and inhomogeneous. The foreign carriers introduced by impurities may also destroy the QAH effect. These make it difficult to detect and maintain the QAH effect at industrial operating temperature (i.e., a few hundred Kelvin). Up to now, extreme conditions including ultralow temperature (<2 K) are still required to observe the QAH effect. In addition, QAH insulators with $|C| > 1$ are not well explored and most of these studies are limited to toy model analysis [21–23].

Recently, a state-of-the-art chemical technology to atomically disperse metal atoms onto/into supporting matrix materials has been widely applied for homogeneous single-atom catalysis [24,25]. Stimulated by this technology, here we predict that the 5*d* transition metal W (tungsten) can be regularly distributed in a porous 2D metal halide normal insulator InI_3 (indium iodide), which is denoted as W@InI_3. Using first-principles calculations, we prove that the W@InI_3 monolayer is an experimentally feasible QAH insulator with strong homogeneous out-of-plane ferromagnetism. Each W^{4+} cation is spin polarized and shows a large magnetic moment of 2 μ_B. They prefer a ferromagnetic (FM) coupling with a high Curie temperature (T_c = ∼160 K), estimated by both Monte Carlo simulation and the magnon excitation model. Most strikingly, we find that it is expected to show a high-temperature QAH effect with a topologically nontrivial band gap (56 meV) and $|C| = 2$. This is verified by calculating the band structure of a W@InI_3 nanoribbon, which gives two linearly dispersed gapless states. These states are found to be localized near the edge of the nanoribbon. In addition, we calculate its

*Author to whom correspondence should be addressed: jianzhou@mail.xjtu.edu.cn

†ekan@njust.edu.cn

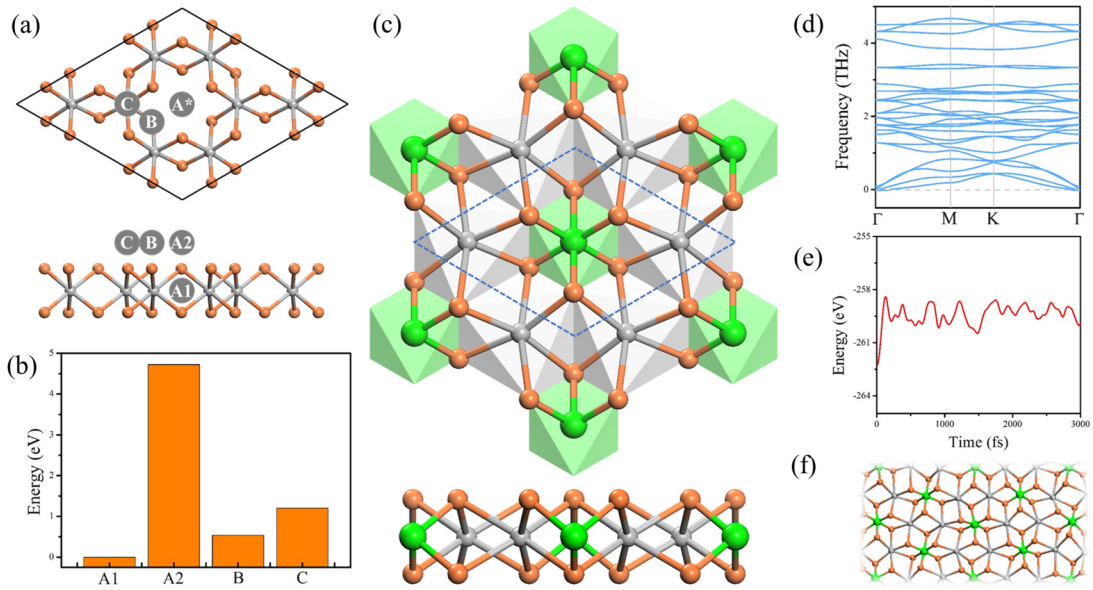

FIG. 1. (a) Four absorption sites (A1, A2, B, and C) of W in the InI_3 monolayer. (b) Relative energy per W for each adsorption configuration. (c) Top and side view of the optimized $W@InI_3$ monolayer. Green, gray, and orange balls represent W, In, and I atoms, respectively. (d) Phonon dispersion along a high-symmetry k path. (e) Total energy as a function of time from *ab initio* molecular dynamics simulation at 300 K. (f) Atomic geometry after molecular dynamics simulation for 3000 fs.

magneto-optical Kerr effect and collective plasmon excitation, which could help for further experimental verifications.

II. COMPUTATIONAL METHODS

We perform first-principles density functional theory (DFT) calculations with Perdew-Burke-Ernzerhof (PBE) [26] treatment of exchange-correlation interaction, as implemented in the Vienna *ab initio* simulation package (VASP) [27]. The core and valence electrons are approximated using the projector augmented wave (PAW) method [28] and a plane-wave basis set with cutoff energy of 400 eV, respectively. To simulate the 2D thin film, a vacuum space of $\sim$15 Å along the z direction is adopted. The first Brillouin zone is represented by a Monkhorst-Pack [29] k mesh of $(8 \times 8 \times 1)$, whose convergence has been tested. The convergence criteria of total energy and force are set to be 1×10^{-5} eV and 0.01 eV/Å, respectively. The SOC effect is included self-consistently with full relativistic pseudopotential. We also have repeated our calculations using the DFT + U method [30] with effective Hubbard U value of 0.5, 1.0, 1.5, 2.0, and 2.5 eV for W-d electrons and using HSE06 hybridized functional. The topological QAH effect feature does not change (see the Supplemental Material [31] for details). To simulate the nanoribbon electronic behavior, we fit the low-energy band dispersion by using maximally localized Wannier functions (MLWFs) as implemented in the WANNIER90 code [32]. The phonon calculations were performed by using the PHONOPY code [33] combined with the density functional perturbation theory method in VASP. The *ab initio* molecular dynamical (AIMD) simulations are performed by using a $(3 \times 3 \times 1)$ supercell under a Nosé-Hoover thermostat at 300 K.

III. RESULTS

A. Geometric structure and stability

Group-III metal halide crystals (e.g., $AlCl_3$ [34] and $InBr_3$ [35]) have been widely used in the chemical industry. To introduce strong SOC, here we choose the nonmagnetic normal insulator InI_3 monolayer (electronic band gap of $\sim$1.9 eV [31]) as the matrix material. To determine the optimal adsorption configuration of W embedded in the InI_3 monolayer, we have considered four possible adsorption sites, namely, the hollow (A1), hollow-top (A2), I-top (B), and In-top (C) sites [Fig. 1(a)]. The results [Fig. 1(b)] show that the A1 configuration is lower in energy than the A2, B, and C configurations by 4.72, 0.54, and 1.20 eV per W, respectively. Thus W atoms prefer to absorb at the hollow site (A1) of the InI_3 monolayer. This is to similar to our previous work of a Li atom adsorbed in a $CrBr_3$ monolayer [36]. Figure 1(c) shows the optimized structure of the $W@InI_3$ (formula unit: In_2WI_6) monolayer, which belongs to the $P\bar{3}1m$ layer group. Each W atom is coordinated to six I ligands with a W-I bond length of 2.77 Å. The lateral lattice constant is 8.07 Å, larger than that of the pristine InI_3 monolayer (7.51 Å). To explore its feasibility in experiment, we calculated its formation energy $E_f = (E_{\mathrm{W@InI3}} - 2\mu_{\mathrm{In}} - \mu_W - 6\mu_I)/9$, where $E_{\mathrm{W@InI3}}$ is the total energy of $W@InI_3$; the chemical potentials μ_{In}, μ_{W}, and μ_{I} are taken from the bcc-In, W crystal, and iodine solid, respectively. The calculated E_f is -0.27 eV/atom. We also calculated the binding energy ($E_b = E_{\mathrm{W@InI3}} - E_W - E_{\mathrm{InI3}}$) of an isolated W atom embedded into the InI_3 monolayer. The E_b is -7.15 eV per W. The phonon dispersion shows no imaginary frequencies [Fig. 1(d)], confirming its dynamical stability. Its thermal stabilities are explored by the AIMD simulations [Fig. 1(e)]. No structural phase transition is observed after 3000 fs of simulations at 300 K [Fig. 1(f)].

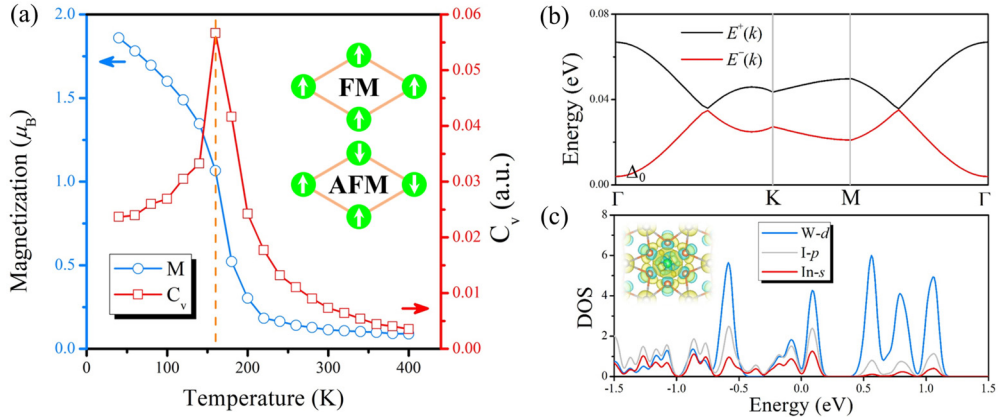

FIG. 2. (a) Average magnetization (M) and specific heat (C_v) as a function of temperature from Monte Carlo simulations. Insets: ferromagnetic (FM) and antiferromagnetic (AFM) spin orders. (b) Magnon dispersion. (c) Projected density of states. The Fermi level is set to 0. Inset: charge difference of W on InI_3 monolayer. Yellow and cyan isosurfaces represent charge accumulation and depletion, respectively.

These facts imply that the W@InI_3 could be feasible in experiments.

B. Magnetic configuration and magnetic behavior under finite temperature

In the W@InI_3, the formal oxidation state of W (valence configuration of $5d^4 6s^2$) is +4; thus two electrons remain on each W atom. These two W-d electrons occupy the t_{2g} orbitals derived from the octahedral crystal field, generating a magnetic moment of $2\,\mu_B$ per unit cell. By using a (2×2) supercell which contains four magnetic W atoms, we calculate the total energy of FM and antiferromagnetic (AFM) configurations [inset of Fig. 2(a)]. The FM pattern is found to be energetically favored over the AFM pattern with an exchange energy ($E_{ex} = E_{AFM} - E_{FM}$) of 56.5 meV per W. When including SOC in our calculations, this E_{ex} is reduced by ~16% ($E_{ex} = 47.2$ meV per W). We calculate its magnetocrystalline anisotropy energy. The out-of-plane magnetic alignment (along the z direction) is energetically lower than when the magnetic axis lies in the xy plane by 3.8 meV per unit cell.

Because of the large magnetocrystalline anisotropy, here we use a simplified nearest-neighbor XXZ Heisenberg model to describe its magnetic behavior. The Hamiltonian reads

$$\hat{H} = -\frac{J}{2}\sum_{\langle i,j\rangle} \vec{S}_i \cdot \vec{S}_j - \frac{\lambda}{2}\sum_{\langle i,j\rangle} S_i^z \cdot S_j^z.$$

The J and λ are exchange parameter and out-of-plane magnetization parameter, respectively. Note that in the current case, $S = 1$. The summation runs over all the nearest-neighbor pairs (i, j). The energies of out-of-plane FM (E_{FM-z}), AFM (E_{AFM-z}) state, and in-plane FM state (E_{FM-x}) can be expressed as

$$E_{FM-z} = E_0 - 3J - 3\lambda, \quad E_{AFM-z} = E_0 + J + \lambda,$$
$$E_{FM-x} = E_0 - 3J,$$

where E_0 is the total energy without magnetic couplings. From the calculated total energy of different magnetic configurations by the DFT + SOC method, we obtain $J = 10.5$ meV and $\lambda = 1.3$ meV. We then perform Monte Carlo (MC) simulations to estimate its T_c. A (30×30) hexagonal spin lattice containing 900 spin sites is used. During the simulations, each spin is rotated randomly in all directions. The average magnetization per site and specific heat [$C_v = (\langle E^2\rangle - \langle E\rangle^2)/k_B T^2$] are taken after the system reaches its equilibrium state at a given temperature. From Fig. 2(a) one observes that T_c is ~160 K (dashed vertical line). At this temperature, the average magnetic moment M drops from its initial $S(=1)$ to ~$S/2$.

These ferromagnetic 2D materials with out-of-plane magnetic easy axis are very interesting theoretically and experimentally owing to the successful synthesis of CrI_3 [37,38] and $Cr_2Ge_2Te_6$ [39] thin films. A detailed understanding of the low-temperature magnetic behavior of the W@InI_3 monolayer would be useful for further analyses. We therefore use the quantum mechanical treatment, i.e., the linear spin wave approximation, to study the magnon excitation of this system [40]. This could also allow us to study the spin wave related thermal and topological properties [41–43]. To do this, we use Holstein-Primakoff representation [44],

$$S_i^+ = \sqrt{2S}\sqrt{1 - \frac{b_i^\dagger b_i}{2S}}\, b_i \sim \sqrt{2S} b_i,$$
$$S_i^- = \sqrt{2S} b_i^\dagger \sqrt{1 - \frac{b_i^\dagger b_i}{2S}} \sim \sqrt{2S} b_i^\dagger,$$
$$S_i^z = S - b_i^\dagger b_i,$$

where b_i and $b_i^\dagger$ are magnon annihilation and creation operators, respectively. Under low temperature, $S_z \sim S$, the Hamiltonian can be written as

$$\hat{H} = \begin{bmatrix} 3JS + 3\lambda S & -\frac{J}{2} S f(\mathbf{k}) \\ -\frac{J}{2} S f^*(\mathbf{k}) & 3JS + 3\lambda S \end{bmatrix},$$

$$f(\mathbf{k}) = \sum_{i=1}^{6} e^{i\mathbf{k}\cdot\mathbf{d}_i} = 2\cos ak_x + 4\cos\frac{ak_x}{2}\cos\frac{\sqrt{3}ak_y}{2},$$

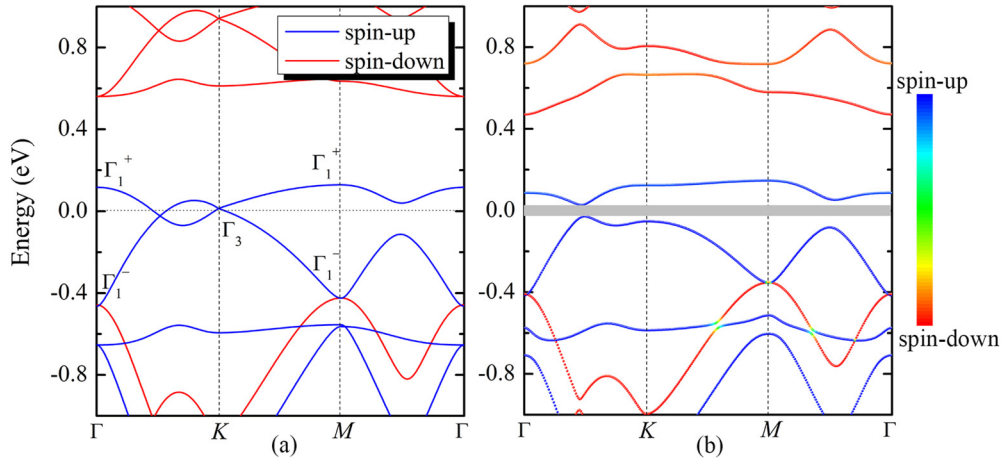

FIG. 3. Band dispersion along the high-symmetry k path, (a) without and (b) with SOC interactions. The symmetry representation is also shown in panel (a). The color map shows the out-of-plane spin component $\langle s_z \rangle$ of each state.

where $\mathbf{d}_i$'s are nearest-neighbor vectors and a is the lattice constant. The energy spectrum of $E^+(k)$ and $E^-(k)$, i.e., the magnon dispersion, is shown in Fig. 2(b). The lower-energy spectrum near the Γ point ($k \to 0$) can be extended to be

$$E^-(\mathbf{k}) = 3\lambda S + \frac{J}{2}S\left[(ak_x)^2 + 2\left(\frac{a}{2}k_x\right)^2 + 2\left(\frac{\sqrt{3}a}{2}k_y\right)^2\right]$$
$$= 3\lambda S + \frac{3}{4}JS(ak)^2 = \Delta_0 + \rho(ak)^2,$$

where $\Delta_0 = 3\lambda S = 3.9$ meV denotes the spin wave gap and $\rho = 3JS/4 = 7.9$ meV denotes the spin stiffness. Under finite temperature, the magnetization is

$$M = S - \frac{1}{(2\pi)^2}\int_{\mathrm{BZ}} \frac{d^2\mathbf{k}}{e^{\beta M E^-(\mathbf{k})/S} - 1}$$
$$= S - \frac{1}{(2\pi)^2}\int_{\mathrm{BZ}} \frac{Sd^2\mathbf{k}}{\beta M[\Delta_0 + \rho(ak)^2]}.$$

The normalization of the magnon satisfies $\frac{1}{(2\pi)^2}\int_{\mathrm{BZ}} a^2 d^2\mathbf{k} = 2$.

Note that a direct integral of these equations is not straightforward. Since the integral is controlled by $E^-(\mathbf{k})$, its value is dominated by the integral near the Γ point. Thus, following the spirit of the Debye model, we assume that the integral is within a circular region (within a cutoff radius k_c), which provides good approximation of the main behavior [40]. In order to obtain T_c, we need to address when M decreases to an obvious small value. Unfortunately, due to the linear approximation feature in this model, there is no finite temperature solution for $M = 0$. Thus we only consider the critical temperature when M decreases to half of S (i.e., $S/2$, similar to what is found in the Monte Carlo simulation),

$$M = \frac{1}{2}S = S - \frac{1}{(2\pi)^2}\int_{\mathrm{BZ}} \frac{Sa^2d^2\mathbf{k}}{2\beta S[\Delta_0 + \rho(ak)^2]}.$$

After integrating, we yield

$$k_B T_c = \frac{2\pi\rho S}{\ln\frac{\Delta_0 + 8\pi\rho}{\Delta_0}} = \frac{3\pi JS^2}{2\ln\left(1 + \frac{2J\pi}{\lambda}\right)}.$$

This gives $T_c = 145$ K, which is consistent with the result (∼160 K) from MC simulations. The Curie temperature increases as the spin wave gap is increased, similar to what is observed in $Cr_2Ge_2Te_6$ [39].

Generally speaking, the strength of superexchange interaction decreases rapidly as the distance between magnetic sites increases. In this system, the distance between nearest magnetic sites, namely, the W-W distance, is quite large (8.07 Å), which should lead to a very weak magnetic coupling. However, the ferromagnetism is found to be rather strong. To understand this, we plot the projected density of state [Fig. 2(c)]. We find that not only I-p orbitals, but also the In-s orbitals participate in the superexchange process. This is different from recently discovered 2D FM semiconductors such as CrI_3 [37] and $CrGeTe_3$ [39], where only ligand p orbitals are involved in magnetic exchange. From the charge difference [inset of Fig. 2(c)], distinct charge transfers from W to In atoms are observed, which partially occupy the In-s orbital and lead to strong d-s-d hybridizations. Because the s orbital is more broadening than p orbitals, thus the d-s-d superexchange persists for a longer distance.

C. Electronic band dispersion and nontrivial topology analysis

Now we study the topological electronic properties of W@InI_3. Before SOC is included [Fig. 3(a)], we see two bands near the Fermi level which are mainly contributed by the spin-up W-e_2 (d_{xy} and $d_{x2\text{-}y2}$) orbitals. This is different from the conventional QAH effect arising from the hybridization between opposite spin states near the Fermi level. This is owing to the large spin split in the system, so that the spin-down states lie away from the Fermi level. One observes two Dirac cones—one locates at the K point and the other one lies along the $\Gamma \to K$ path. This can be briefly understood by a simple group analysis. Note that the little group of the $\Gamma(K)$ point is D_{3d} (C_{3v}). We find that at both the Γ and M points, the valence and conduction bands have Γ_1^- and Γ_1^+ symmetry, respectively [Fig. 3(a)]. According to group compatibility theory, these two bands must have even times of crossing. Hence, the band crossing along the $\Gamma \to K$ path

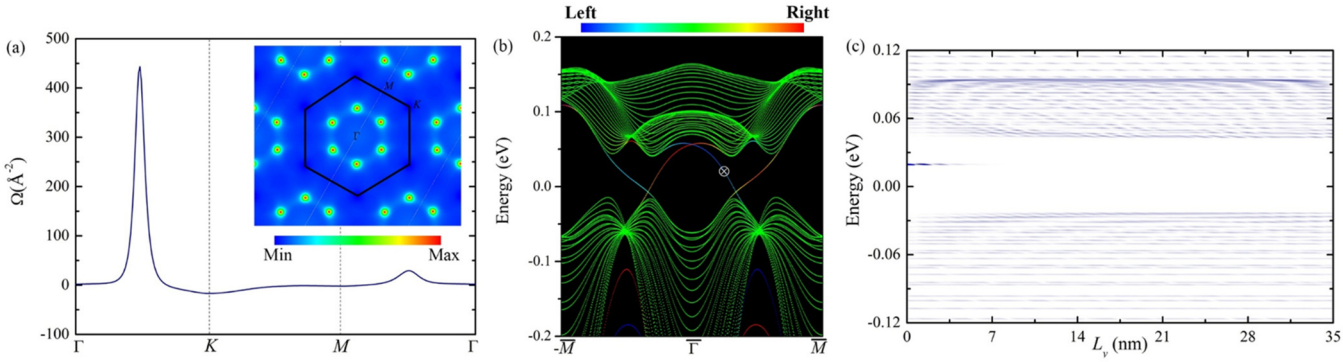

FIG. 4. (a) Berry curvature in the k space. (b) MLWF based tight-binding band structure of nanoribbon, where blue to red colors represent left edge to right edge state contributions, respectively. (c) Local density of state (LDOS) distribution at $k = 1/4 \times (\bar{\Gamma} \to \bar{M})$ of the nanoribbon. One clearly sees a localized edge state inside the bulk band gap, which is indicated in (b) as a white circled cross.

is an accidental degeneracy. These multiple band crossings also suggest a QAH conductance with $C > 1$, once SOC is included.

Since the W-e_2 orbitals have a high magnetic quantum number, the intra-atomic SOC term $\mathbf{L} \cdot \mathbf{S}$ is large (this is also the reason for a large magnetocrystalline anisotropy energy). Hence, one expects that including SOC can induce a large nontrivial band gap. Indeed, as shown in Fig. 3(b), we see a finite band gap opening at the Fermi level. Due to its spatial inversion symmetry, no Rashba effect is observed and the out-of-plane spin component $\langle s_z \rangle$ is not strongly quenched. The direct band gap at the K point is 176 meV, and its global band gap of 56 meV locates along the $\Gamma \to K$ path. Such large band gap suggests that the W@InI_3 monolayer might be a room-temperature QAH insulator.

In order to explore its topological feature, we calculate its k-resolved Berry curvature, $\Omega(k) = i \sum_{E_{nk} \leqslant E_F} \langle \nabla_k u_{nk}| \times |\nabla_k u_{nk}\rangle$, where E_F is the Fermi energy and $|u_{nk}\rangle$ is the periodic part of the Bloch wave function of band n at k, from our first-principles calculations. The summation runs over all occupied bands. The results are shown in Fig. 4(a), where we see one pronounced peak at the finite band gap (along $\Gamma \to K$). Totally there are six such peaks in the first Brillouin zone. Integration of Berry curvature over the first Brillouin zone gives the Chern number, $C = \frac{1}{2\pi} \int_{\mathrm{BZ}} \Omega(k) d^2k = 2$. Thus, our proposed W@$InI_3$ monolayer is indeed a QAH insulator with a finite Chern number. Next, we fit the band dispersion (with SOC) by a tight binding Hamiltonian based on MLWFs. We construct a zigzag edged nanoribbon with ~35 Å width and calculate its band structure [Fig. 4(b)]. One clearly observes two localized metallic states on each edge of the nanoribbon, propagating along opposite directions. This confirms that the Chern number $C = 2$. The localization of such edge state can be quantified from its local density of state (LDOS) [Fig. 4(c)]. We find that the state indicated as the white circled cross (its energy is 0.02 eV above the E_F) is mainly localized within ~2 nm from its edge. The group velocity of this state is $v_g = 9.3 \times 10^4$ m/s.

D. Anomalous Hall conductance and magneto-optical Kerr effect

We then adjust its chemical potential μ (with respect to E_F) and calculate its anomalous Hall conductance, $\sigma_{xy} = Ce^2/h$ [Fig. 5(a)]. A quantized terrace of $2e^2/h$ inside the global band gap is clearly seen. When the chemical potential lies out of the band gap, σ_{xy} drastically decreases to a small value. This curve can be verified by Hall resistance measurement at zero magnetic field in experiments. In addition, recent studies show that magneto-optical measurements, such as Faraday and Kerr rotation effects, provide a fingerprint probe of Hall conductivity. As the quantized Hall transverse current $\sigma_{xy} = Ne/h^2$ actually features the magnetoelectric effect at the low-frequency limit, the optical process at finite frequency offers a direct detection of quantum anomalous Hall scenario [45–47]. In addition, the Faraday and Kerr angles are related to the fine structure constant $\alpha(= 1/137)$. Thus, the observation of them can be critical to verify our predicted material and aid the measurement of α. In order to provide a theoretical prediction, we calculate the optical Hall conductivity for its potential magneto-optical measurement by the Kubo-Greenwood formula [48],

$$\sigma_{\alpha\beta}(\omega) = e^2\hbar \int_{\mathrm{BZ}} \frac{d^2k}{(2\pi)^2} \sum_{n \neq m} (f_{mk} - f_{nk}) \times \frac{\mathrm{Im}\langle \psi_{nk}|\nabla_\alpha|\psi_{mk}\rangle\langle\psi_{mk}|\nabla_\beta|\psi_{nk}\rangle}{(E_{mk} - E_{nk})^2 - (\hbar\omega + i\eta)^2},$$

where f_{nk} is the Fermi-Dirac distribution, $\hbar\omega$ specifies the incident optical energy, and η is an infinitesimal smearing parameter ($\alpha, \beta = x, y$). Then, we can quantify the field induced magneto-optic Kerr effect (MOKE). For simplicity, the incident light propagation is assumed normal to the surface, and no reflection is considered. The complex polar Kerr angles can be obtained by [49,50]

$$\theta_K + i\eta_K = \frac{2Z_0 d\sigma_{xy}}{1 - (n_s + Z_0 d\sigma_{xx})^2},$$

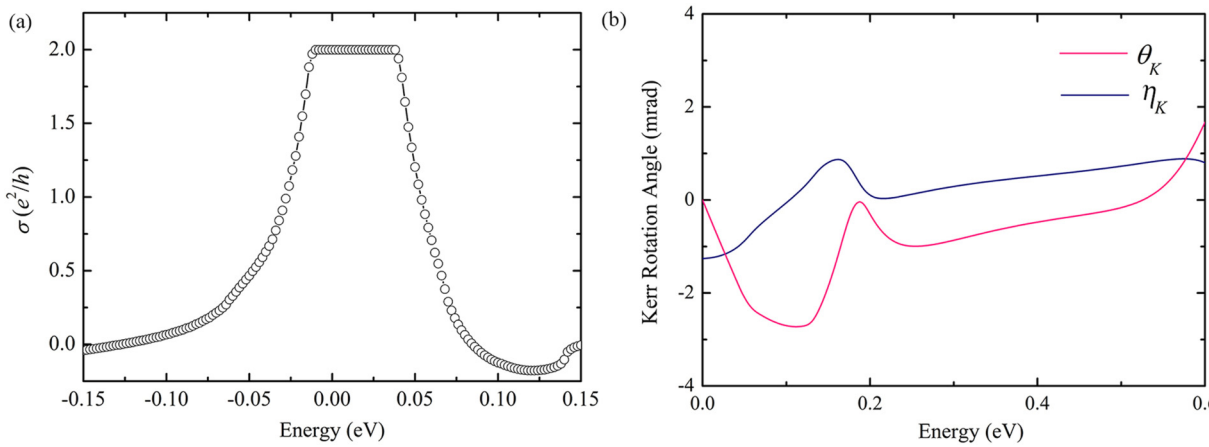

FIG. 5. (a) Integrated anomalous Hall conductance σ_{xy} as function of chemical potential, where a terrace of $\sigma = 2\,e^2/h$ appears around the Fermi level. (b) Calculated MOKE with respect to incident energy.

where the real part (θ_K) and complex part (η_K) are the rotation angle of the major axis of the linearly polarized light and the ratio of the minor to the major axis of the light, respectively. n_s is the refractive index of the substrate (e.g., SiO_2, taken to be 1.5 in this study), $Z_0 = 377\,\Omega$ is the impedance of free space, and $d = 3.22$ Å is the thickness of the system. From Fig. 5(b), we see fluctuation of both Kerr angles with respect to incident optical energy. The η_K reaches its maximum of 1 mrad when $\hbar\omega = 0.18$ eV, and the minimum value of θ_K is -2.8 mrad when $\hbar\omega = 0.12$ eV. These can be measured in magneto-optical experiments.

E. Plasmonic behavior of linear band dispersion of a W@InI_3 nanoribbon

The collective mode of massless Dirac-type plasma is explicitly nonclassical ($\hbar$ dependent) in all dimensions, rather than commonly studied metals and doped semiconductors [51]. According to Das Sarma and Hwang [51], the electron energy loss spectrum (EELS) in linear band dispersion is also related to the dimensionless fine structure constant. Owing to the robustness of Dirac dispersion in edge states of topological materials, measurement of their EELS could aid us to study these facts. Besides, the quantum anomalous Hall effect is time-reversal symmetry broken, which may provide more features than that in time-reversal symmetric Dirac dispersion (such as graphene). Unfortunately, the plasmonic response of QAH insulator nanoribbons using EELS is rarely discussed. Here, we study the collective plasmon excitation and the screening spectrum. The noninteracting polarization function can be calculated by the Lindhard function,

$$\Pi(q,\omega) = -\frac{1}{2\pi}\int dk \sum_{n,m}(f_{n,k} - f_{m,k+q}) \times \frac{|\langle u_{m,k+q}\,|\,u_{n,k}\rangle|^2}{E_{n,k} - E_{m,k+q} + \hbar\omega + i\eta},$$

where the integral is performed in the one-dimensional (1D) first Brillouin zone. We use Fermi-Dirac distribution at the temperature at $T = 300$ K, and η is taken to be 0.5 meV. Then, we evaluate the dielectric function within the random phase approximation (RPA),

$$\varepsilon(q,\omega) = 1 + V(q)\Pi(q,\omega),$$

where $V(q) = (2e^2/4\pi\varepsilon_0\varepsilon_r)K_0(qa)$, where relative dielectric constant ε_r is calculated to be 55.8 within RPA. The $K_0(x)$ is the zeroth-order modified Bessel function of the second kind, which can be approximated to be $|\ln(x)|$ for $x \to 0$. The length parameter a characterizes the typical lateral confinement size of the 1D electron system, which is taken as 2 nm as found in LDOS. The nodes of the frequency-dependent dielectric function correspond to the excitation spectrum of the plasmon modes. The real and complex parts of the dielectric function quantify the dispersion and loss of plasmon modes, respectively. The EELS is defined as $\mathcal{L}(q,\omega) = -\mathrm{Im}[1/\varepsilon(q,\omega)]$, which can be used to specify the weight of the plasmon mode.

Figure 6(a) shows the calculated EELS $\mathcal{L}(q,\omega)$ of an n-doped nanoribbon. Due to its symmetry, the EELS along the $+q$ and $-q$ are identical. Thus, we only plot $+q$ results here. By fitting the EELS in the long wavelength limit, we find the cutoff frequency $\omega_p \sim q^{0.87}$ in our system, rather than that of $\sqrt{q}$ in 2D Dirac systems. This agrees with previous theoretical model analysis [51], namely, $\omega_p \sim q|\ln(qa)|$ when the chemical potential is fixed. Moreover, the EELS is more damped when q gets larger, due to larger interband scattering effects. We also shift the chemical potential μ and calculate the $\mathcal{L}(q,\omega)$ with a fixed q [Fig. 6(b)]. According to the previous analytical work [51], the ω_p is proportional to $\sqrt{v_g}$ but not to μ. Consistently, our result shows that ω_p merely remains to be a constant in the vicinity of the Fermi level, and slightly increases when μ approaches the valence bands. These facts would be helpful to identify the Dirac bands feature in experiments.

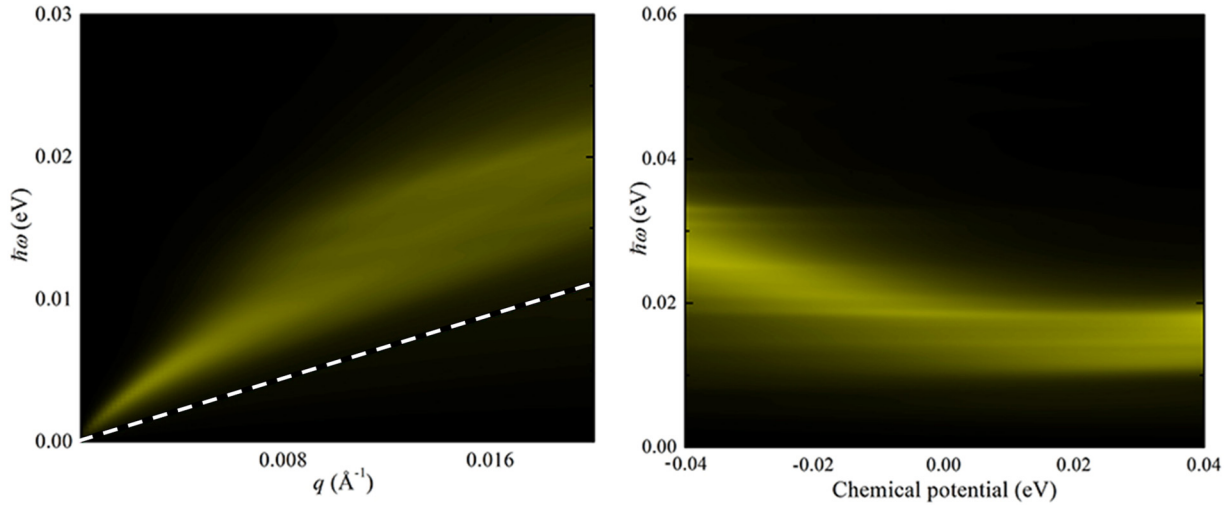

FIG. 6. (a) EELS $\mathcal{L}(q,\omega)$ dispersion of n-doped system with chemical potential $\mu = E_F + 0.2\,\text{eV}$. The area below the white dashed line ($v_g q$) is the single-particle excitation damping region. (b) Calculated EELS $\mathcal{L}(q,\omega)$ with fixed $q = 0.018\,\text{Å}^{-1}$ under different chemical potential relative to Fermi level.

IV. CONCLUSION

In summary, we use first-principles calculations to predict an intrinsic QAH insulator with strong homogeneous out-of-plane ferromagnetism, based on the experimentally realizable atomic dispersion of W into the metal halide InI_3 monolayer. We show that the pores in the InI_3 film can firmly absorb W atoms, exhibiting a uniform trigonal FM lattice. Both Monte Carlo and magnon excitation analyses based on the Heisenberg spin interaction model show an observable high T_c of ~160 K. The W-e_2 orbitals form several Dirac cones at the K point and along the $\Gamma \rightarrow K$ path. Intrinsic SOC would open a global band gap of 56 meV, with a Chern number of $|C| = 2$. This can be further demonstrated by calculating its metallic edge state. In order to facilitate future experiments, we also calculated its magneto-optical Kerr effect and its collective plasma excitation modes, which could also help to measure the fine structure constant. Our study provides opportunities for realizing a robust QAH effect and feasible 2D FM Chern insulators, which will be of interest for future spintronics.

ACKNOWLEDGMENTS

E.K. is supported by the NSFC (Grants No. 51522206, No. 11774173, and No. 11574151), by PAPD, the Fundamental Research Funds for the Central Universities (Grant No. 30915011203), and by New Century Excellent Talents in University (Grant No. NCET-12-0628).

[1] F. D. M. Haldane, Model for a Quantum Hall Effect without Landau Levels: Condensed-Matter Realization of the "Parity Anomaly", Phys. Rev. Lett. **61**, 2015 (1988).

[2] J. G. Checkelsky, R. Yoshimi, A. Tsukazaki, K. S. Takahashi, Y. Kozuka, J. Falson, M. Kawasaki, and Y. Tokura, Trajectory of the anomalous Hall effect towards the quantized state in a ferromagnetic topological insulator, Nat. Phys. **10**, 731 (2014).

[3] H. Weng, R. Yu, X. Hu, X. Dai, and Z. Fang, Quantum anomalous Hall effect and related topological electronic states, Adv. Phys. **64**, 227 (2015).

[4] C.-X. Liu, S.-C. Zhang, and X.-L. Qi, The Quantum anomalous Hall effect: Theory and experiment, Annu. Rev. Condens. Matter Phys. **7**, 301 (2016).

[5] R. Yu, W. Zhang, H. J. Zhang, S. C. Zhang, X. Dai, and Z. Fang, Quantized anomalous Hall effect in magnetic topological insulators, Science **329**, 61 (2010).

[6] Z. F. Wang, Z. Liu, and F. Liu, Quantum Anomalous Hall Effect in 2D Organic Topological Insulators, Phys. Rev. Lett. **110**, 196801 (2013).

[7] S.-C. Wu, G. Shan, and B. Yan, Prediction of Near-Room-Temperature Quantum Anomalous Hall Effect on Honeycomb Materials, Phys. Rev. Lett. **113**, 256401 (2014).

[8] G. Xu, J. Wang, C. Felser, X.-L. Qi, and S.-C. Zhang, Quantum anomalous Hall effect in magnetic insulator heterostructure, Nano Lett. **15**, 2019 (2015).

[9] L. Dong, Y. Kim, D. Er, A. M. Rappe, and V. B. Shenoy, Two-Dimensional π-Conjugated Covalent-Organic Frameworks as Quantum Anomalous Hall Topological Insulators, Phys. Rev. Lett. **116**, 096601 (2016).

[10] P. Zhou, C. Q. Sun, and L. Z. Sun, Two dimensional antiferromagnetic Chern insulator: $NiRuCl_6$, Nano Lett. **16**, 6325 (2016).

[11] C. Huang, J. Zhou, H. Wu, K. Deng, P. Jena, and E. Kan, Quantum anomalous Hall effect in ferromagnetic transition metal halides, Phys. Rev. B **95**, 045113 (2017).

[12] H. P. Wang, W. Luo, and H. J. Xiang, Prediction of high-temperature quantum anomalous Hall effect in two-dimensional transition-metal oxides, Phys. Rev. B **95**, 125430 (2017).

[13] C.-Z. Chang, J. Zhang, X. Feng, J. Shen, Z. Zhang, M. Guo, K. Li, Y. Ou, P. Wei, L.-L. Wang, Z.-Q. Ji, Y. Feng, S. Ji, X. Chen, J. Jia, X. Dai, Z. Fang, S.-C. Zhang, K. He, Y. Wang *et al.*, Experimental observation of the quantum anomalous Hall effect in a magnetic topological insulator, Science **340**, 167 (2013).

[14] X. Kou, S.-T. Guo, Y. Fan, L. Pan, M. Lang, Y. Jiang, Q. Shao, T. Nie, K. Murata, J. Tang, Y. Wang, L. He, T.-K. Lee, W.-L. Lee, and K. L. Wang, Scale-Invariant Quantum Anomalous Hall Effect in Magnetic Topological Insulators beyond the Two-Dimensional Limit, Phys. Rev. Lett. **113**, 137201 (2014).

[15] C.-Z. Chang, W. Zhao, D. Kim, Y. H. Zhang, B. A. Assaf, D. Heiman, S.-C. Zhang, C. Liu, M. H. W. Chan, and J. S. Moodera, High-precision realization of robust quantum anomalous Hall state in a hard ferromagnetic topological insulator, Nat. Mater. **14**, 473 (2015).

[16] I. Lee, C. K. Kim, J. Lee, S. J. L. Billinge, R. Zhong, J. A. Schneeloch, T. Liu, T. Valla, J. M. Tranquada, G. Gu, and J. C. Séamus Davis, Imaging Dirac-mass disorder from magnetic dopant atoms in the ferromagnetic topological insulator $Cr_x(Bi_{0.1}Sb_{0.9})_{2-x}Te_3$, Proc. Natl. Acad. Sci. USA **112**, 1316 (2015).

[17] E. O. Lachman, A. F. Young, A. Richardella, J. Cuppens, H. R. Naren, Y. Anahory, A. Y. Meltzer, A. Kandala, S. Kempinger, Y. Myasoedov, M. E. Huber, N. Samarth, and E. Zeldov, Visualization of superparamagnetic dynamics in magnetic topological insulator, Sci. Adv. **1**, e1500740 (2015).

[18] X. Feng, Y. Feng, J. Wang, Y. Ou, Z. Hao, C. Liu, Z. Zhang, L. Zhang, C. Lin, J. Liao, Y. Li, Li.-Li. Wang, S.-H. Ji, X. Chen, X. Ma, S.-C. Zhang, Y. Wang, K. He, and Q.-K. Xue, Thickness dependence of the quantum anomalous Hall effect in magnetic topological insulator films, Adv. Mater. **28**, 6386 (2016).

[19] S. F. Qi, Z. H. Qiao, X. Z. Deng, E. D. Cubuk, H. Chen, W. G. Zhu, E. Kaxiras, S. B. Zhang, X. H. Xu, and Z. Y. Zhang, High-Temperature Quantum Anomalous Hall Effect in n-p Codoped Topological Insulators, Phys. Rev. Lett. **117**, 056804 (2016).

[20] Y. Ou, C. Liu, G. Jiang, Y. Feng, D. Zhao, W. Wu, X.-X. Wang, W. Li, C. Song, L.-L. Wang, W. Wang, W. Wu, Y. Wang, K. He, X.-C. Ma, and Q.-K. Xue, Enhancing the quantum anomalous Hall effect by magnetic codoping in a topological insulator, Adv. Mater. **30**, 1703062 (2018).

[21] F. Wang and Y. Ran, Nearly flat band with Chern number $C = 2$ on the dice lattice, Phys. Rev. B **84**, 241103 (2011).

[22] Y.-F. Wang, H. Yao, C.-D. Gong, and D. N. Sheng, Fractional quantum Hall effect in topological flat bands with Chern number two, Phys. Rev. B **86**, 201101 (2012).

[23] M. Trescher and J. Bergholtz, Flat bands with higher Chern number in pyrochlore slabs, Phys. Rev. B **86**, 241111 (2012).

[24] B. Qiao, A. Wang, X. Yang, L. F. Allard, Z. Jiang, Y. Cui, J. Liu, J. Li, and T. Zhang, Single-atom catalysis of CO oxidation using Pt_1/FeO_x, Nat. Chem. **3**, 634 (2011).

[25] P. Liu, Y. Zhao, R. Qin, S. Mo, G. Chen, L. Gu, D. M. Chevrier, P. Zhang, Q. Guo, D. Zhang, B. Wu, G. Fu, and N. Zheng, Photochemical route for synthesizing atomically dispersed palladium catalysts, Science **352**, 797 (2016).

[26] J. P. Perdew, K. Burke, and M. Ernzerhof, Generalized Gradient Approximation Made Simple, Phys. Rev. Lett. **77**, 3865 (1996).

[27] G. Kresse and J. Hafner, *Ab initio* molecular dynamics for liquid metals, Phys. Rev. B **47**, 558 (1993).

[28] P. E. Blöchl, Projector augmented-wave method, Phys. Rev. B **50**, 17953 (1994).

[29] H. J. Monkhorst and J. D. Pack, Special points for Brillouin-zone integrations, Phys. Rev. B **13**, 5188 (1976).

[30] S. L. Dudarev, G. A. Botton, S. Y. Savrasov, C. J. Humphreys, and A. P. Sutton, Electron-energy-loss spectra and the structural stability of nickel oxide: An LSDA + U study, Phys. Rev. B **57**, 1505 (1998).

[31] See Supplemental Material at http://link.aps.org/supplemental/10.1103/PhysRevB.98.115424 for results from GGA + U and HSE06 calculations, and properties of pristine InI_3 monolayer.

[32] A. A. Mostofi, J. R. Yates, G. Pizzi, Y. S. Lee, I. Souza, D. Vanderbilt, and N. Marzari, An updated version of WANNIER90: A Tool for Obtaining Maximally Localised Wannier Functions, Comput. Phys. Commun. **185**, 2309 (2014).

[33] A. Togo and I. Tanaka, First principles phonon calculations in materials science, Scr. Mater. **108**, 1 (2015).

[34] K. Sasvári, On the crystal structure of $AlCl_3$, Acta Phys. **9**, 195 (1958).

[35] T. Staffel and G. Z. Meyer, Z. Anorg. Allg. Chem. **563**, 27 (1988).

[36] C. Huang, Y. Du, H. Wu, H. Xiang, K. Deng, and E. Kan, Prediction of Intrinsic Ferromagnetic Ferroelectricity in a Transition-Metal Halide Monolayer, Phys. Rev. Lett. **120**, 147601 (2018).

[37] B. Huang, G. Clark, E. Navarro-Moratalla, D. R. Klein, R. Cheng, K. L. Seyler, D. Zhong, E. Schmidgall, M. A. McGuire, D. H. Cobden, W. Yao, D. Xiao, P. Jarillo-Herrero, and X. Xu, Layer-dependent ferromagnetism in a van der Waals crystal down to the monolayer limit, Nature **546**, 270 (2017).

[38] D. Zhong *et al.*, Van der Waals engineering of ferromagnetic semiconductor heterostructures for spin and valleytronics, Sci. Adv. **3**, e1603113 (2017).

[39] C. Gong, L. Li, Z. Li, H. Ji, A. Stern, Y. Xia, T. Cao, W. Bao, C. Wang, Y. Wang, Z. Q. Qiu, R. J. Cava, S. G. Louie, J. Xia, and X. Zhang. Discovery of intrinsic ferromagnetism in two-dimensional van der Waals crystals, Nature **546**, 265 (2017).

[40] J. L. Lado and J. Fernández-Rossier, On the origin of magnetic anisotropy in two dimensional CrI_3, 2D Mater. **4**, 035002 (2017).

[41] R. Chisnell, J. S. Helton, D. E. Freedman, D. K. Singh, R. I. Bewley, D. G. Nocera, and Y. S. Lee, Topological Magnon Bands in a Kagome Lattice Ferromagnet, Phys. Rev. Lett. **115**, 147201 (2015).

[42] R. Cheng, S. Okamoto, and D. Xiao, Spin Nernst Effect of Magnons in Collinear Antiferromagnets, Phys. Rev. Lett. **117**, 217202 (2016).

[43] V. A. Zyuzin and A. A. Kovalev, Magnon Spin Nernst Effect in Antiferromagnets, Phys. Rev. Lett. **117**, 217203 (2016).

[44] T. Holstein and H. Primakoff, Field dependence of the intrinsic domain magnetization of a ferromagnet, Phys. Rev. **58**, 1098 (1940).

[45] R. Nandkishore and L. Levitov, Polar Kerr Effect and Time Reversal Symmetry Breaking in Bilayer Graphene, Phys. Rev. Lett. **107**, 097402 (2011).

[46] K. N. Okada, Y. Takahashi, M. Mogi, R. Yoshimi, A. Tsukazaki, K. S. Takahashi, N. Ogawa, M. Kawasaki, and Y. Tokura, Terahertz spectroscopy on Faraday and Kerr rotations in a quantum anomalous Hall state, Nat. Commun. **7**, 12245 (2016).

[47] A. L. Yeats, P. J. Mintun, Y. Pan, A. Richardella, B. B. Buckley, N. Samarth, and D. D. Awschalom, Local optical control of ferromagnetism and chemical potential in a topological insulator, Proc. Natl. Acad. Sci. USA **114**, 10379 (2017).

[48] H. Ebert, Magneto-optical effects in transition metal systems, Rep. Prog. Phys. **59**1665 (1996).

[49] R. Valdes Aguilar, A. V. Stier, W. Liu, L. S. Bilbro, D. K. George, N. Bansal, L. Wu, J. Cerne, A. G. Markelz, S. Oh, and N. P. Armitage, Terahertz Response and Colossal Kerr Rotation from the Surface States of the Topological Insulator Bi_2Se_3, Phys. Rev. Lett. **108**, 087403 (2012).

[50] N. Sivadas, S. Okamoto, and D. Xiao, Gate-Controllable Magneto-optic Kerr Effect in Layered Collinear Antiferromagnets, Phys. Rev. Lett. **117**, 267203 (2016).

[51] S. Das Sarma and E. H. Hwang, Collective Modes of the Massless Dirac Plasma, Phys. Rev. Lett. **102**, 206412 (2009).